Observation of summertime upwelling off the eastern and northeastern coasts of Hainan Island, China

Peigen Lin[1] · Jianyu Hu[1] · Quanan Zheng[1,2] · Zhenyu Sun[1] · Jia Zhu[1]

Abstract Using cruise observations and reanalysis data, this study analyzes the effects of wind, freshwater, and turbulent mixing on the two upwellings: one is off the eastern coast of Hainan Island (HEU) and the other is off the northeastern coast of Hainan Island (HNEU). During the cruise in 2009, the HNEU occurred with southwesterly to southeasterly wind. The relative large values of turbulent kinetic energy dissipation rate and diffusivity estimated from the Thorpe scale indicate that the upwelling water is further uplifted to the surface by strong turbulent mixing in the HNEU region. But the HEU was not observed under the southeasterly wind. During the cruise in 2012, the HNEU disappeared in the upper layer with freshwater covered and southeasterly wind, while the apparent HEU only accompanied with southwesterly wind. To obtain the general characteristics, we define three types of upwelling patterns, i.e., the intensified HEU, the intensified HNEU, and both HEU and HNEU in one day, using the reanalysis data. The composites of sea surface temperature (SST), wind, and precipitate for each upwelling pattern identify that the HNEU is associated with the prevailing southeasterly wind and can be limited in the lower layer when it is covered by freshwater. But the HEU is mainly driven by southwesterly wind but is not remarkably affected by freshwater.

Responsible Editor: Jörg-Olaf Wolff

✉ Jianyu Hu
   hujy@xmu.edu.cn

[1] State Key Laboratory of Marine Environmental Science, College of Ocean and Earth Sciences, Xiamen University, Xiamen, Fujian 361102, China

[2] Department of Atmospheric and Oceanic Science, University of Maryland, College Park, MD 20742, USA

1 Introduction

Summertime coastal upwelling is one of the most important phenomena in the northern South China Sea. The upwelling over the east shelf of Hainan Island is a significant phenomenon in the northern South China Sea, known as Qiongdong upwelling (see Xie et al. 2012 for a review). In fact, the upwelling includes two upwelling components (e.g., Li et al. 2012): (1) Upwelling off the eastern coast of Hainan Island (or Hainan eastern upwelling, HEU) and (2) upwelling off the northeastern coast of Hainan Island (or Hainan northeastern upwelling, HNEU).

The HEU has been widely studied. The maximum vertical velocity of the upwelling calculated by simplified momentum equation is approximately 3×10^{-5} m s^{-1} (Han et al. 1990; Guo et al. 1998). The summer southwesterly monsoon is considered as the driving force for the upwelling (Jing et al. 2011). The Ekman pumping induced by the local wind stress curl is also responsible for the formation of the upwelling (Jing et al. 2009). By estimating the Ekman transport and Ekman pumping in the upwelling region, Wang et al. (2013) identified that 33 % of the total wind-driven upwelling is due to Ekman pumping, the rest is due to Ekman transport. Wind not only induces the upwelling locally, but also forces the large-scale circulation of the South China Sea to affect the upwelling (Su and Pohlmann 2009). Su et al. (2011) predicted that the wind-driven upwelling is associated with cross-shelf circulation according to the Burger number. The number is about 0.96 nearby the Hainan Island, which means that the balance of the shoreward transport

and the surface offshore transport exists in the interior layer rather than in the bottom layer. They also pointed out that the freshwater from river discharges only inhibits the upwelling in the nearshore region. Besides, the vertical mixing caused by the internal waves plays a positive role in the upwelling intensification and the varying coastline determines the upwelling location (Su and Pohlmann 2009).

However, a few studies have analyzed the HNEU specifically. The local wind not only generates the upwelling (Li 1990), but also controls its variability (Li et al. 2012). Since a special bottom topography is associated with an upwelling-favorable cross-shelf circulation (e.g., Gan et al. 2009), the bottom topography off the eastern and northeastern coasts of Hainan Island interacting with current may be significant in the process of HNEU (Li et al. 2012; Song et al. 2012). Particularly, Lin et al. (2016) diagnosed that the along-isobath barotropic pressure gradient force mainly intensities the HNEU. Similarly, the HNEU is also enhanced by the large-scale circulation of the South China Sea in summer (Li et al. 2012). In addition to wind and current, eddies and tides were also reported as important factors affecting the HNEU (Yu 1987; Song et al. 2012).

However, the characteristics, especially the differences, of the HEU and HNEU have not been well understood due to the limited evidences. The analysis and comparison of the HEU and HNEU may help to better understand their detailed processes. This study aims to explore these upwelling processes using the methods and data sources described in Section 2. The results are given in Section 3 and discussed in Section 4. Section 5 is the conclusions.

2 Data and methods

2.1 Hydrographic observation and reanalysis data

The two cruises were carried out during July 16 – August 15, 2009 and during July 29 – August 21, 2012, respectively. Temperature and salinity data were conducted off the eastern and northeastern coasts of Hainan Island (Fig. 1) during the two cruises using the Seabird SBE 911 and 917 CTD (Conductivity-Temperature-Depth) profilers. The instrument accuracies of conductivity, temperature, and pressure are 3×10^{-4} S/m, 1×10^{-3} °C, and 1 dbar, respectively.

The real-time wind data were measured from the meteorological station (Wind Monitor-MA) onboard. The threshold sensitivity and the available range of the instrument are 1.1 and 0–100 m s^{-1}, respectively. The 10-s wind data were block-averaged into 5-min intervals. In addition, a daily blended wind dataset with a resolution of 0.25°, during summers (June, July and August) from 2006 to 2012 covering the time of the two cruises, is provided by the National Climatic Data Center (http://www.ncdc.noaa.gov/). This wind data are generated by blending multiple-satellite observations and re-analysis products (Zhang et al. 2006).

The daily and high-resolution ($1/20° \times 1/20°$) sea surface temperature (SST) data are produced by the Operational SST and Sea Ice Analysis (OSTIA) system. The SST reanalysis data are assimilated from satellite and in situ data, which are available from the website of Group for High Resolution Sea Surface Temperature (https://www.ghrsst.org/). To match the timescale of the blended wind data, we also choose the SST data for the summers in 2006–2012 (644 SST images).

The daily precipitation data are from the Version 7 Tropical Rainfall Measuring Mission (TRMM) product 3B42 (ftp://
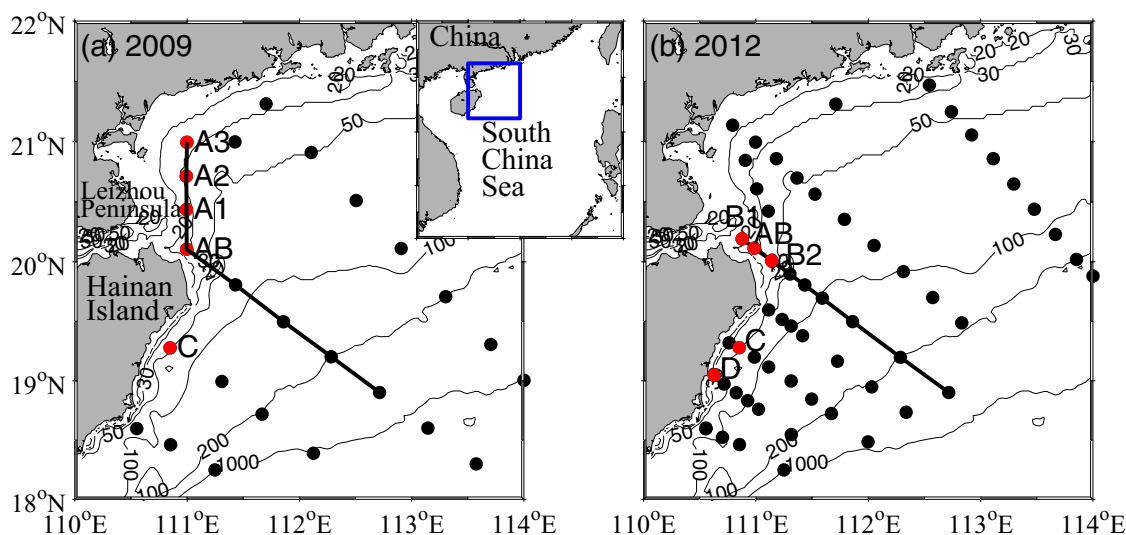
Fig. 1 Sampling stations (*black dots*) including the selected stations (*red dots*) and two transects (*black lines*) for two cruises during the summers of 2009 (**a**) and 2012 (**b**). Note that station AB and station C were covered both in 2009 and in 2012. Bathymetric contours are in meters

meso-a.gsfc.nasa.gov/pub). The data, in a horizontal resolution of 0.25° × 0.25°, combine multi-satellite microwave-IR estimates (Huffman et al. 2007). Similarly, the precipitation data for the summers in 2006–2012 are chosen.

2.2 Methods

Potential density σ_θ is computed to estimate vertical overturning according to the Thorpe scale (L_T, Thorpe 1977). In turn, the turbulent kinetic energy (TKE) dissipation rate is empirically estimated from

$$\varepsilon = 0.64 L_T^2 N^3, \tag{1}$$

where N is the vertical-sorted buoyancy frequency from potential density profiles (Dillon 1982; Nash et al. 2007;

Alford et al. 2011; Klymak et al. 2011). From both TKE dissipation rate ε and buoyancy frequency N, the diffusivity is computed by $K_z = \Gamma \varepsilon N^{-2}$, where Γ is an efficiency parameter, commonly set as 0.2 (Osborn 1980). The noise of data is removed according to the CTD instrument resolution and the run length test (Galbraith and Kelley 1996; Stansfield et al. 2001).

The upwelling extent is identified from daily SST images using the fuzzy c-means clustering (FCM, see Sousa et al. 2008 for details), which has been successfully used in upwelling identification in many studies (e.g., Chen et al. 2012). As a fuzzy pixel classification method, the FCM aims to partition image pixels into c (the number) fuzzy clusters through iteratively approximating the minima of the objective function. Figure 2c shows an example of FCM algorithm with $c = 4$ clusters applied to the SST
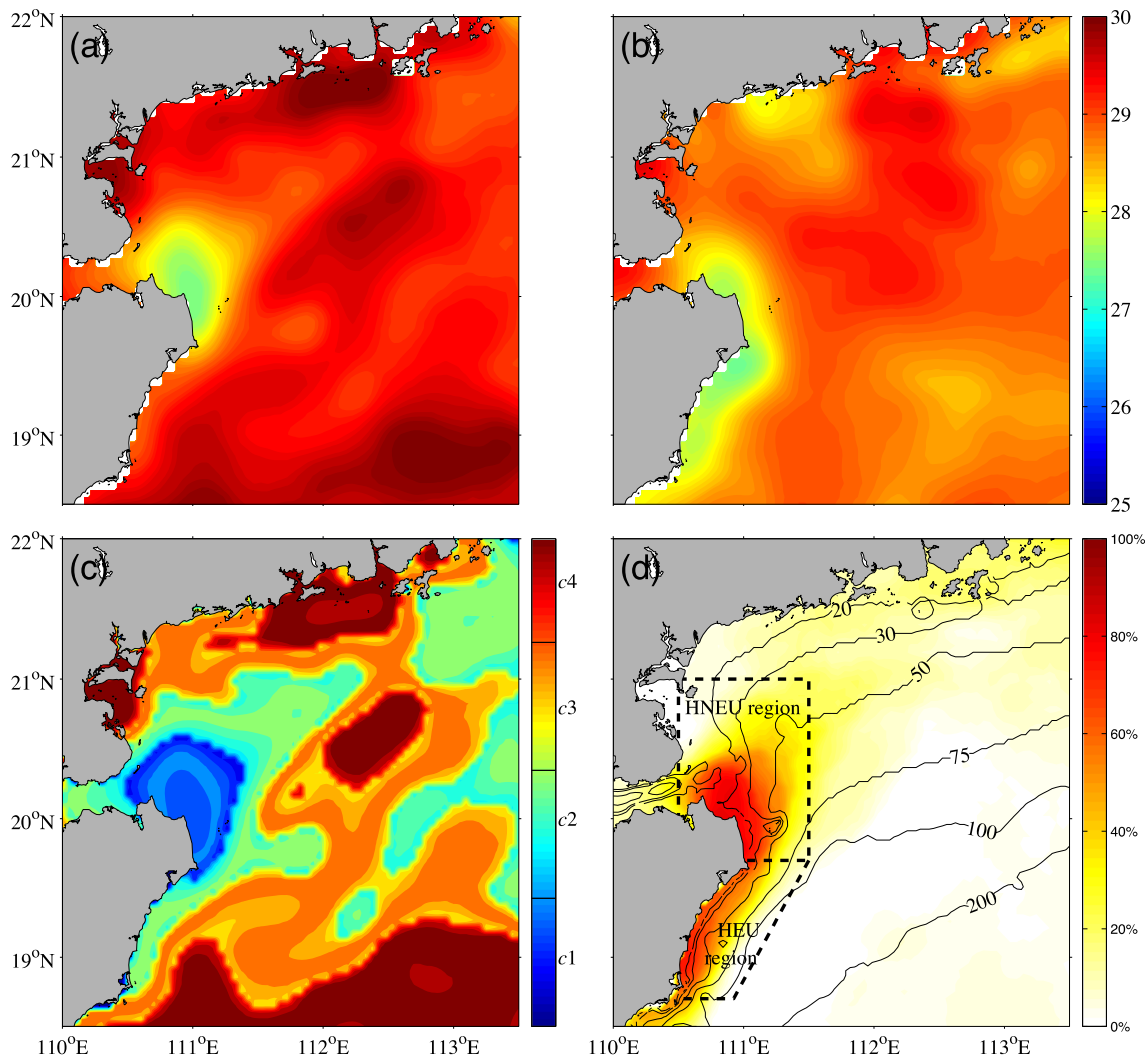
Fig. 2 The daily SST image on July 24, 2009 (**a**) and August 14, 2012 (**b**) from OSTIA. **c** The corresponding FCM 4-partition image on July 24, 2009, in which colored *blue* and *dark red* are upwelling areas and non-upwelling areas, respectively. **d** The probability distribution of the upwelling identified from the FCM algorithm. The HEU and HNEU regions (*dashed boxes*) in **d** are the regions for computing upwelling indexes. Bathymetric contours are in meters

image (Fig. 2a) on July 24, 2009 corresponding to the cruise mission time. A relatively cold upwelling area is located in the shelf off the northeastern coast of Hainan Island and represented in blue (cluster $c1$) in the FCM image. Similarly, the non-upwelling regions with higher SST are colored by dark red (cluster $c4$).

Based on the all FCM images, the probability of upwelling in each SST pixel is calculated as the ratio of the number of upwelling days to the total number of SST images (644 days). To facilitate the upwelling analysis, we define the regions according to the probability distribution of upwelling and name them as HEU region and HNEU region, respectively (Fig. 2d, dashed boxes).

UI_{NE} (UI_E) is short for the upwelling index of HNEU (HEU) region which is defined as the difference of averaged SST between the HNEU (HEU) region and non-upwelling region for each SST image. Larger value represents more intensified upwelling.

3 Results

3.1 Distributions of the upwelling

Apparently, a region with relatively low temperature and high salinity was located off the northeastern coast of Hainan Island at a depth of 5 m during the 2009 cruise (Fig. 3a, c). The central temperature and salinity are 26.5 °C and 33.6 psu, respectively. In contrast, during the 2012 cruise, the low temperature and high-salinity region (central temperature of 26 °C and the salinity of 33.6 psu) was over the shelf off the eastern coast of Hainan Island (Fig. 3b, d). This difference of upwelling patterns well matches with the SST images from reanalysis data as shown in Fig. 2a, b. At the depth of 20 m, the nearshore area was occupied by the low temperature and high-salinity water during both the cruises in 2009 and 2012 (Fig. 4).
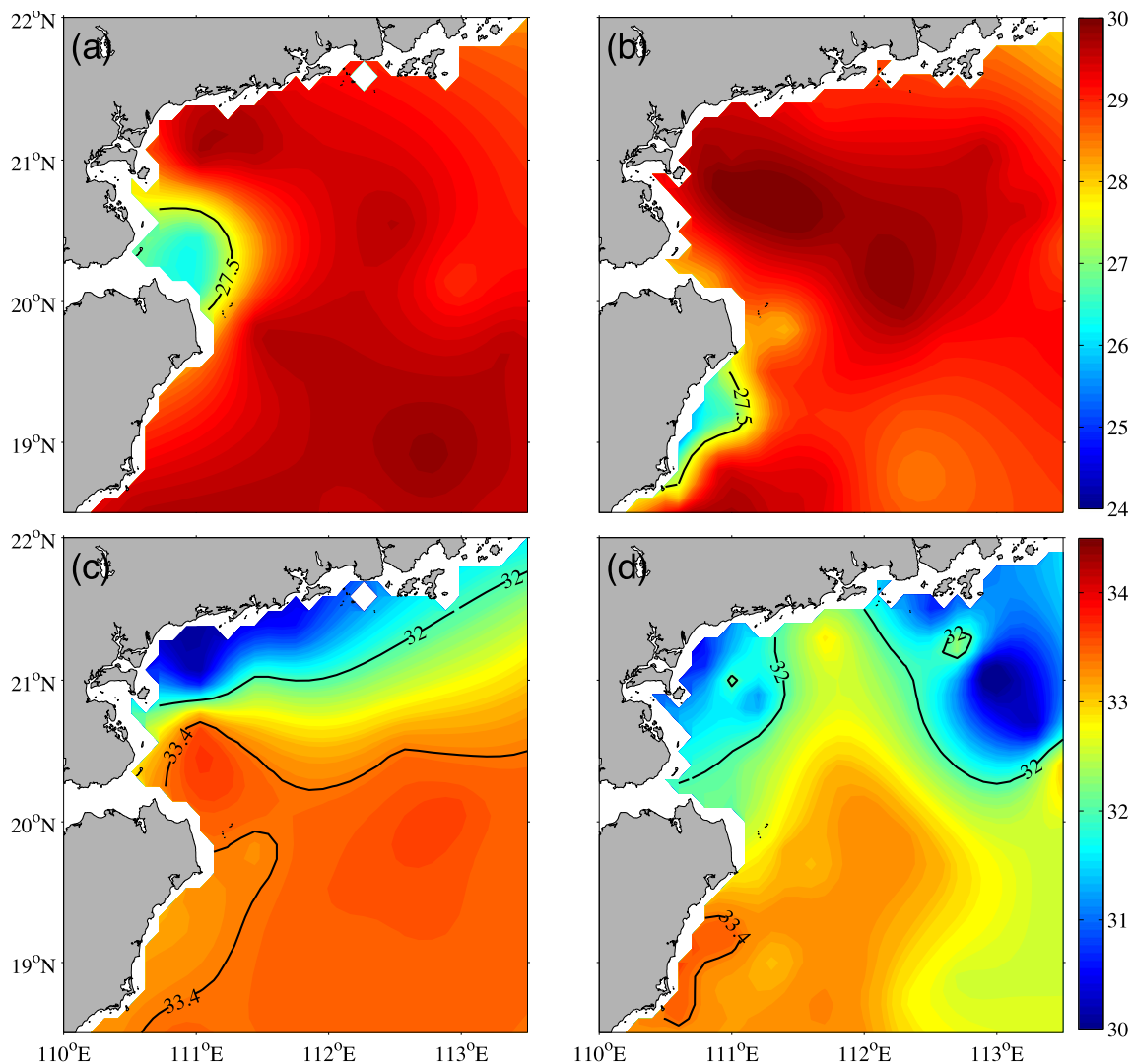
Fig. 3 Distributions of temperature (°C) (**a**, **b**) and salinity (psu) (**c**, **d**) at a depth of 5 m during summer cruises in 2009 (**a**, **c**) and 2012 (**b**, **d**)
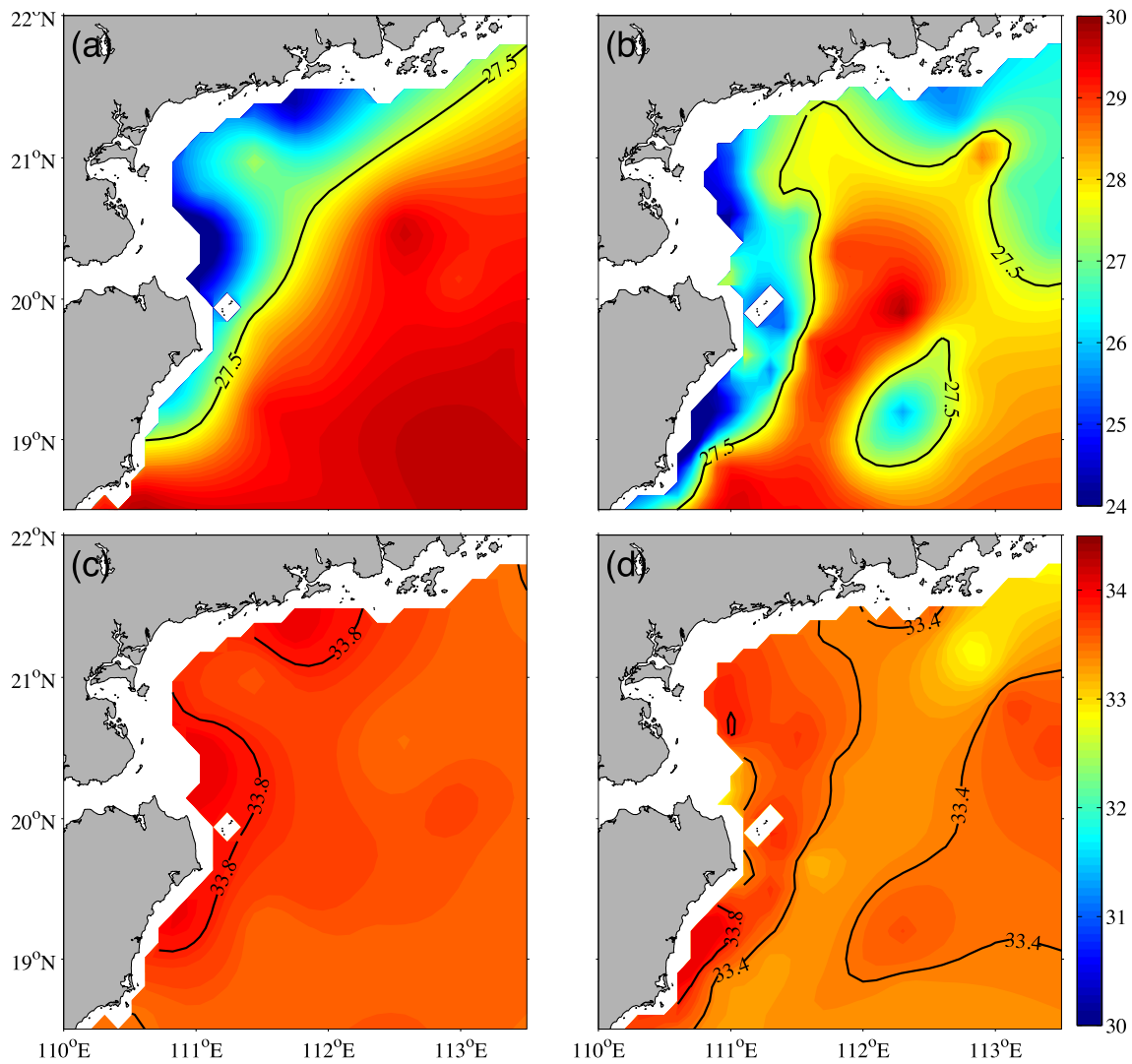
Fig. 4 Same as Fig. 3 except at a depth of 20 m

3.2 Effect of wind

3.2.1 Case analysis

To verify the effect of wind, we perform a case analysis of the HNEU and HEU based on the cruise observations. A scatter diagram v (meridional component) against u (zonal component) from the real-time wind data is shown in Fig. 5. Clearly, in the HEU region, winds were southeasterly (cross-shore) during the cruise mission in summer 2009 so the HEU did not exist, while winds were southwesterly (alongshore) during the cruise mission in summer 2012, thus a strong HEU appeared. In the HNEU region, the most scattered points gather in the first quadrant of the coordinate system (southwesterly wind) during the 2012 cruise when the HNEU was not apparent. Winds swung between southwesterly and southeasterly during the 2009 cruise, but the HNEU was still observable in the upper layer.

The wind-related upwelling process can be more clearly identified through comparing wind conditions and the vertical
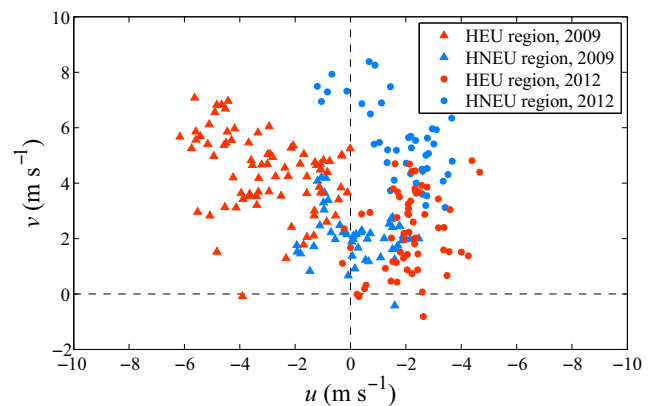

Fig. 5 The u-v scatter plot of 10 min-averaged wind data from measurements in the HEU region (*red*) and HNEU region (*blue*) during the cruises in 2009 (*triangles*) and 2012 (*dots*)
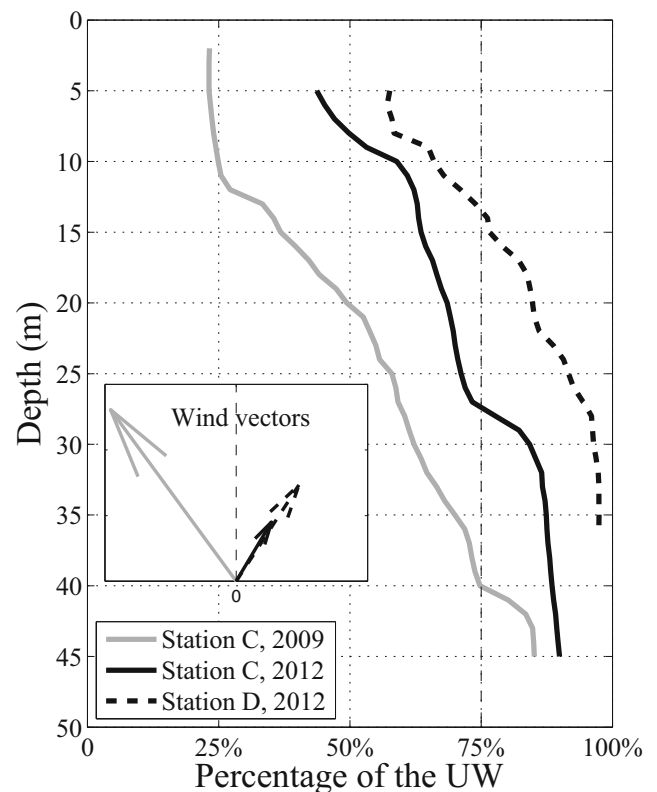
structure of water masses. The water mass distribution is analyzed using triangle of mixing method summarized by Mamayev (1975) (see appendix for detail). Based on the θ-S diagram (Fig. 6), the percentages of the mixing ratio among the three water masses, the freshwater (FW), the upwelling water (UW), and the sea surface water (SW) are estimated. The θ-S diagram includes the data of all nearshore stations (depth <50 m) and offshore stations (depth >200 m) in the study regions in cruises of 2009 and 2012.

For the HEU, station C covered in two cruises and station D only in 2012 (located at the center of the HEU) were selected (Fig. 1). At station C of 2009, UW was lower than 75 % in the upper 40 m (Fig. 7, gray line). In contrast, the water mass with 75 % UW was uplifted to 28 m depth at the corresponding station in 2012 (Fig. 7, black line). Accordingly, the southeasterly wind (6.5 m s^{-1}) and southwesterly wind (2.1 m s^{-1}) were blowing at station C during the 2009 and 2012 cruises, respectively. It indicates that southwesterly wind is conductive to generation of the HEU. At the center of the HEU, the UW (>50 %) dominated the whole water column of station D in 2012 (Fig. 7, black dashed line), where the averaged wind had similar direction but larger magnitude (3.5 m s^{-1}) comparing to the condition at station C in the cruise. It shows that the HEU is not only generated but also intensified by the southwesterly wind, which is in line with the previous studies (e.g., Jing et al. 2011).

To see effects of wind on the HNEU, we select the nearshore stations (in HNEU region) in corresponding transects in 2009 and 2012 (Fig. 1). In Fig. 8c, the vertical structure of UW in 2009 shows that the percentage of UW near the bottom layer at stations A2, A1, and AB is more than 75 %. In particular, at station A1, the 75 % contour uplifted toward 20 m
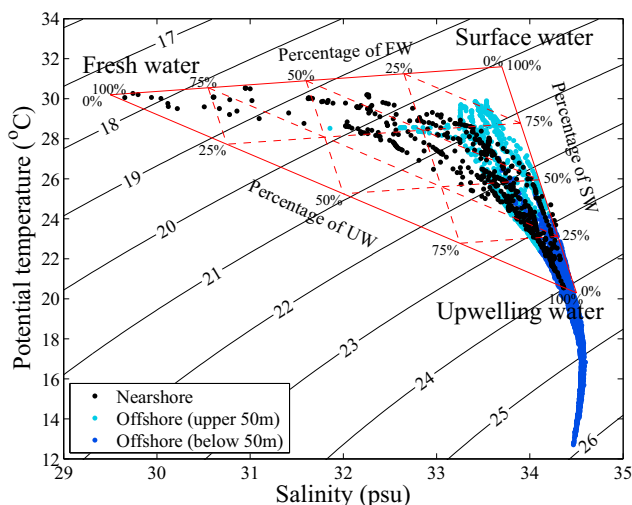
Fig. 7 Profiles of the percentage of mixing ratio of UW at the corresponding station C in 2009 (gray line) and 2012 (black line) and station D in 2012 (black dash line), with corresponding wind vectors, respectively

depth and the 50 % contour reached to the subsurface. The averaged winds were southwesterly except at station A2 (Fig. 8a). It is different in 2012 that the water mass with over 75 % UW was limited below 30 m (Fig. 8d), while wind was southwesterly and two times larger in magnitude (Fig. 8b). Thus, the strong southwesterly wind may not be favorable to the HNEU in this case, which is further discussed in Section 4.

3.2.2 General characteristics

Here, we apply the long-term reanalysis data to provide general features of the HEU and HNEU. Three types of upwelling patterns are distinguished from the 644 SST images: (1) Intensified HEU, defined as the upwelling pattern in the days that the UI$_E$ is higher than the mean value plus the half of one standard deviation (0.5 SD) while UI$_{NE}$ is less than the mean value minus 0.5 SD (namely, UI$_E$ > mean + 0.5 SD and UI$_{NE}$ < mean − 0.5 SD); (2) Intensified HNEU, defined as the upwelling pattern in the days when UI$_{NE}$ > mean + 0.5 SD and UI$_E$ < mean − 0.5 SD; and (3) Both intensified HEU and HNEU in one day, defined as the upwelling pattern in the days when UI$_{NE}$ > mean + 0.5 SD and UI$_E$ > mean + 0.5 SD. It is noted that the range 0.5 SD is used to avoid the number of samples being not large enough to analyze. Interestingly, the

Fig. 6 Potential temperature (θ) versus salinity (S) for the nearshore stations (depth <50 m, black dots) and the offshore stations (depth >200 m) of which the water column is divided into two components: upper 50 m (light blue dots) and below 50 m (dark blue dots). A red triangle of mixing borders the θ-S scatter plot of the nearshore stations
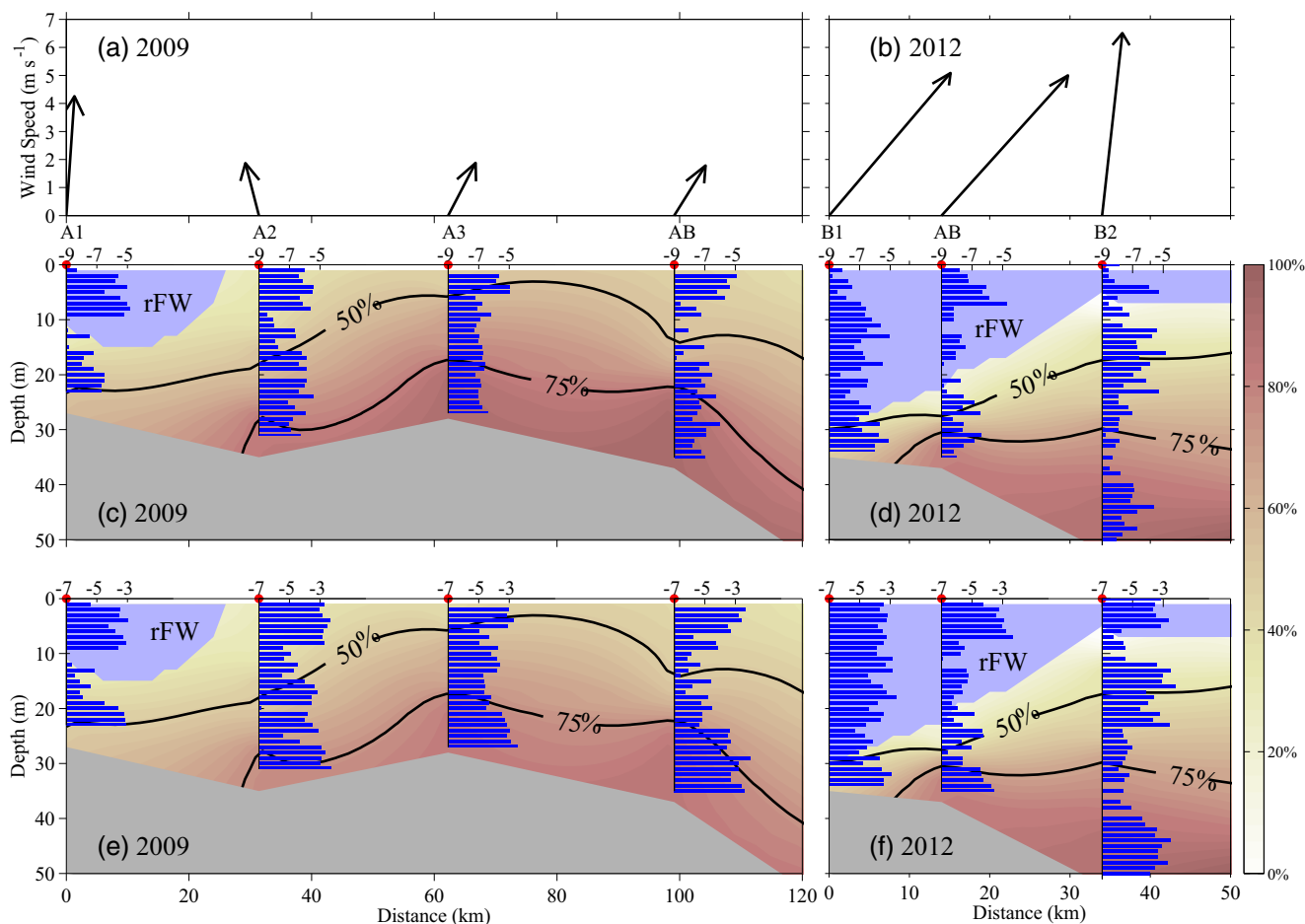
Fig. 8 Wind vectors at the stations in HNEU region during the cruises in 2009 (**a**) and 2012 (**b**). Sectional distributions of the rFW (*light blue areas*), the mixing percentage of the UW (*contours*), and the logarithmic TKE dissipation rates $\log_{10}[\varepsilon(\mathrm{W\ kg^{-1}})]$ (*blue bars*) at nearshore stations along the selected transects in HNEU region in 2009 (**c**) and 2012 (**d**). **e** and **f** are same as **c** and **d** except for the logarithmic vertical diffusivity $\log_{10}[K_z\ (\mathrm{m^2\ s^{-1}})]$ (*blue bars*)

third upwelling pattern occurs in 113 days, while the only intensified HEU pattern is in 29 days and the only intensified HNEU pattern is in 18 days.

The composite of SST superimposed by the composite of wind for each upwelling pattern is shown in Fig. 9. For the intensified HEU pattern (Fig. 9a), the southwesterly wind is upwelling-favorable in the HEU region, while southerly-southwesterly wind prevails in the HNEU region. The averaged $\mathrm{UI_E}$ slowly increases from roughly 0.8 to over 1.0 °C with the steady southwesterly wind continuing for 7 days before this upwelling pattern (Fig. 10a, red vectors and bars). However, in the HNEU region, the averaged wind is southeasterly on former 4 days (from −7 to −3 days in Fig. 10a, blue vectors and bars) while the averaged $\mathrm{UI_{NE}}$ is stably around 0.8 °C, and then transfers to be southwesterly corresponding to the apparently decreasing of the $\mathrm{UI_{NE}}$. It agrees with the results from in situ data.

The southeasterly wind dominates the HNEU region for the intensified HNEU pattern (Fig. 9b). However, the HEU disappears under the southeasterly wind. From 7 days

before the upwelling pattern, corresponding to the continuously southeasterly wind, the $\mathrm{UI_{NE}}$ keeps the level with small increase (Fig. 10b). On the contrary, the $\mathrm{UI_E}$ drops rapidly while the alongshore wind is replaced by the cross-shore wind. Statistically, it again highlights the important role of southwesterly wind in the HEU formation, and illustrates that southeasterly wind benefits the intensified HNEU.

During the upwelling pattern of both HEU and HNEU in one day (Fig. 9c), wind is nearly southerly in both HEU and HNEU regions. It seems that both the intensified HEU and HNEU patterns develop from this upwelling pattern according to the variations of upwelling indexes and wind shown in Fig. 10. Acting as a middle pattern of the upwelling processes, this upwelling pattern transfers to the intensified HNEU pattern when the HNEU keeps its level under the southeasterly wind but the HEU is inhibited by shoreward wind. On the other hand, the upwelling pattern becomes the intensified HEU pattern if HEU is intensified by alongshore wind but HNEU is weakened.
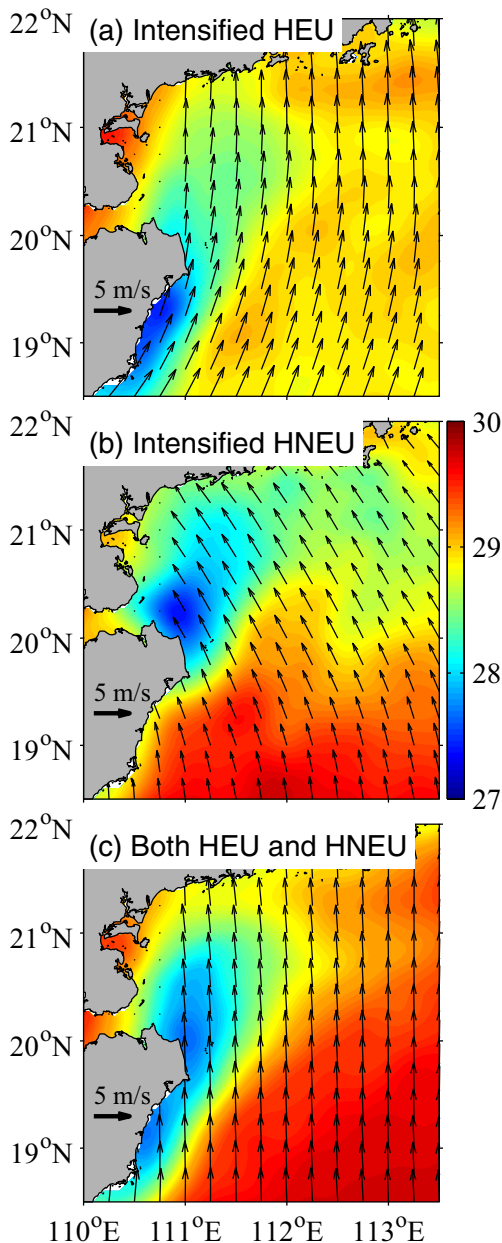
Fig. 9 The composites of SST and wind for the three types of upwelling patterns: Intensified HEU (**a**), Intensified HNEU (**b**), and both HEU and HNEU in one day (**c**)

3.3 Effects of freshwater

3.3.1 Case analysis

The contribution of freshwater is taken account to the HNEU as well as to the HEU. In Fig. 3, one can see that the water with relatively low salinity covered a larger area of the HNEU region during the 2012 cruise than during the 2009 cruise. Sectional distributions of salinity and potential density (σ_θ - 1000 kg m^{-3}) at the two selected transects are shown in Fig. 11. In these two transects, there are five stations covered

in both cruises. Three other stations along the 30 m isobath are only conducted in 2009 and four other stations are only in 2012. The shoreward-lifting isopycnals elevated from off-shore toward the nearshore region, and outcropped to the surface between 50 and 100 km of the transect in 2009 (Fig. 11a). In 2012, the isopycnals uplifted toward the subsurface at roughly 150 km where low potential density water was covered on the surface (Fig. 11b). In the θ-S diagram (Fig. 6), the scatters of the nearshore stations (black dots) do not overlay the ones of the offshore stations (dark and light blue dots) in the area where the percentage of FW is more than 20 %. It means that the water mass represented in this area does not originate from offshore regions. Therefore, in this study, the water mass mixing with over 20 % FW is considered as being related to FW (rFW).

We construct the sectional distributions of the rFW in the HNEU region during the 2009 and 2012 cruises (Fig. 8c, d). In 2009, the rFW only occupied the upper 10-m layer between stations A1 and A2, while the UW was apparently uplifted at station A3 (Fig. 8c) as mentioned before. In 2012, the influence extent of the rFW was upper 5 m at station B2, and extended to upper 30 m at station B1, whereas 75 % contour of UW is limited below 30 m (Fig. 8d). We compare the condition at station AB covered in both cruises. The maximum buoyancy frequency (N_{max}^2) was 1.0×10^{-2} s^{-2} at a depth of 27 m, matching the effective depth of the rFW in 2012 (Fig. 8d), and was over three times larger than that in 2009 ($N_{max}^2 = 3.5 \times 10^{-3}$ s^{-2}) (not shown). The water mass mixing about 75 % UW was uplifted to the depth where the buoyancy frequency was close to the maximum. This co-occurrence suggests that the HNEU can be limited by the strong stratification due to freshwater in the upper layer.

But the low-salinity water was not detected in the HEU region during either cruise. The maximum percentages of FW at the three selected stations (station C in 2009, stations C and D in 2012) were roughly 16, 13, and 9 %.

3.3.2 General characteristics

To further clarify the general effect of freshwater, we also computed the composite of precipitation for each upwelling pattern (Fig. 12). Apparently, for the intensified HEU pattern (Fig. 12a), high mean precipitation is over the north of 20° N, especially on the Leizhou Peninsula (close to 20 mm h^{-1}). But there is virtually no precipitation on average in the HEU region. We can expect that the high precipitation brings considerable freshwater to the shelf off the eastern coast of the Leizhou Peninsula and in the HNEU region. The precipitation pattern is close to the freshwater distribution in the 2012 cruise (Fig. 3d), when the HNEU disappeared in the surface. Associated with the intensified HNEU (Fig. 12b), no precipitation is over the land and shelf nearby or in the HNEU
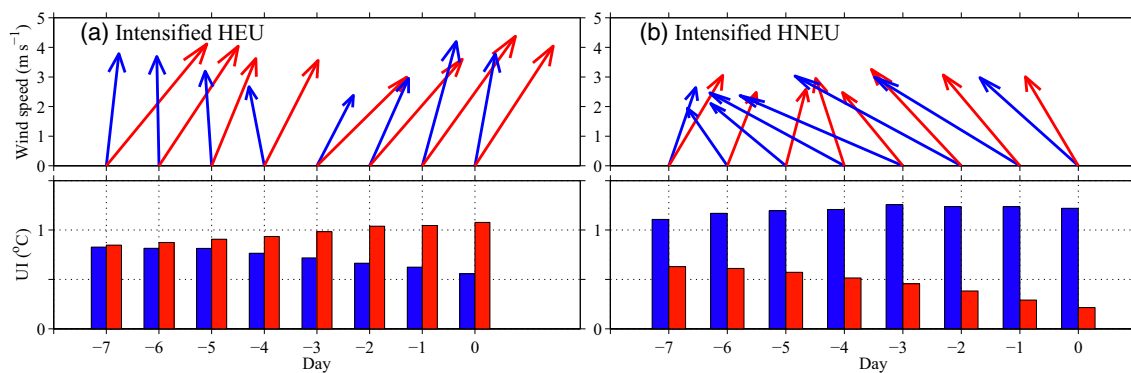
Fig. 10 The variation of the averaged upwelling index (*bars*) and the corresponding averaged wind vectors in the HEU (*red*) and HNEU (*blue*) region 1–7 days before the day of the two upwelling patterns (day 0): intensified HEU (**a**) and intensified HNEU (**b**)

region. But the HEU region has small precipitation. In addition, for the upwelling pattern of both HEU and HNEU in one day, composited precipitation is small over lands (less than 10 mm h^{-1}), and close to zero in the sea areas (Fig. 12c).

It again reveals the freshwater plays a negative role in the HNEU. But owing to its small magnitude (shown in both in situ and reanalysis data) in the HEU region, freshwater does not actually affect the HEU.

3.4 Effects of turbulent mixing

For dynamic processes, the northern South China Sea is featured by tides and high-frequency nonlinear internal waves, which are important in turbulence generation and diapycnal mixing (Liu and Lozovatsky 2012). The deep water has higher potential density and is diffused to the upper layer, even to the surface, by mixing processes (Jiang et al. 2011). It is worth noting that the study regions are mainly located on the


Fig. 11 Sectional distributions of salinity (*color*) and potential density (σ_θ -1000 kg m^{-3}, *contours*) during cruises in 2009 (**a**) and 2012 (**b**). Station AB was covered in both cruises

nearshore shelf (water depth <50 m) (Fig. 2d). Therefore, turbulent mixing should be taken into account.

Turbulence is usually generated by variable atmospheric forcing in the surface mixed layer and tidal flows in the bottom boundary layer. The profiles of TKE dissipation rate ε and vertical diffusivity K_z at selected stations in the HNEU region are shown in Fig. 8c–f. In the surface mixed layer, defined as the upper 5-m layer in the stations based on the vertical distribution of ε, the maximum ε and K_z were as large as 10^{-5} W kg^{-1} and 10^{-3} m^2 s^{-1}. In the deeper layer, ε and K_z had large variations among stations. At station A1 in 2009, the ε and K_z were nearly uniform (Fig. 8c, e), which is associated with more UW reaching to the surface. In other words, since the strong turbulent mixing throughout the water column, with relatively high averaged dissipation rate $\varepsilon=1.1\times10^{-6}$ W kg^{-1} and vertical diffusivity $K_z=2.6\times10^{-3}$ m^2 s^{-1}, the uplifted deeper water was further diffused up to the surface. However, at most stations, ε and K_z were small at roughly 10 m depth where the diffusing process was weak. Although large ε and K_z were observed at station B1 in 2012, the dominated rFW in the whole water column retreated the upwelling process (Fig. 8d, f) owing to the strong stratification (analyzed in Section 3.3). These results show that strong turbulent mixing throughout the water column is able to further diffuse the UW to the upper layer (even surface) on the condition that the UW has been uplifted.

The turbulent mixing condition of the HEU is represented by vertical structures of ε and K_z at the three selected stations in the HEU region (Fig. 13). As the condition in the HNEU region (Fig. 8), the maximum magnitudes of ε and K_z existed in the surface layer in HEU stations. At station C, ε, and K_z were higher in 2009 than those in 2012 throughout the water column, but the HEU was apparent during the 2012 cruise rather than during the 2009 cruise. In 2012, the ε and K_z at the HEU center (station D) were higher than those at station C. Particularly in the surface and bottom layers, the ε and K_z at station D were close to the orders of 10^{-5} W kg^{-1} and 10^{-3} m^2 s^{-1}, respectively. It suggests that the turbulent mixing does not directly generate the HEU, but further intensifies the generated HEU.
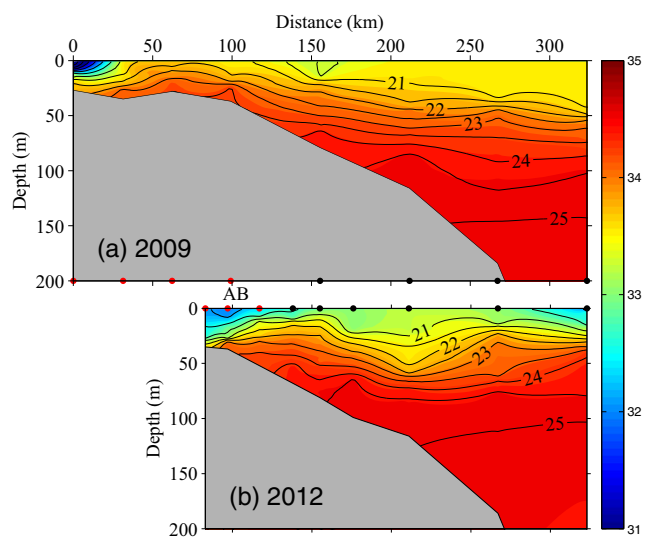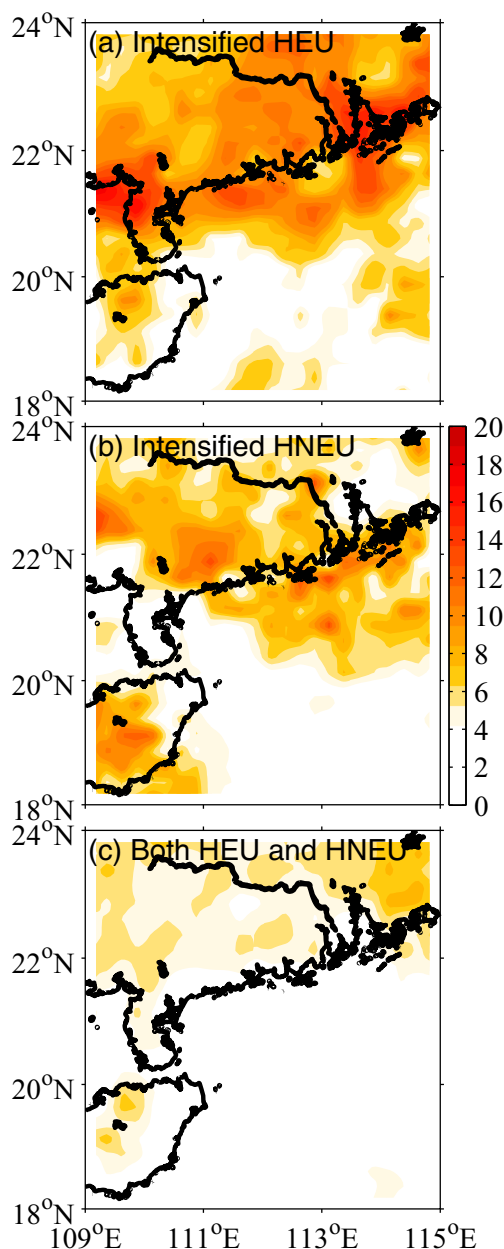
Fig. 12 The composites of precipitation (mm h^{-1}) for the three types of upwelling patterns: Intensified HEU (**a**), intensified HNEU (**b**) and both HEU, and HNEU in one day (**c**)

4 Discussion

Different to the HEU, the HNEU is not a classical wind-driven coastal upwelling based on the Ekman process. Remind that the upwelling pattern of both HEU and HNEU in one day is the most frequent upwelling pattern (in 113 days). We suspect that HEU and HNEU are related in most of the intensified upwelling period. As reported by Lin et al. (2016), the

along-isobath wind causes the HEU, meanwhile drives current to form the HNEU through flow-topography interaction. In this study, however, the HNEU was not obvious when southwesterly wind blew (Figs. 8b and 9a) in either in situ data or reanalysis data. As noted in Section 3.1, in the 2012 cruise, the HNEU disappeared in the surface, but was apparent at a depth of 20 m (Figs. 3 and 4). By comparing the effects of wind and freshwater on the HNEU, the covered freshwater, rather than the southwesterly wind, can be the key factor that stops the deep water uplifting to the surface.

As shown in Section 3.2, the intensified HNEU pattern is associated with southeasterly wind (Fig. 9). Linking with the deduction that freshwater has a negative effect on the HNEU, we suspect that the southeasterly wind may weaken the southward extension of freshwater that originates from the north. This is consistent with Lentz and Fewings (2012) who pointed out that the shoreward wind is a substantial term that drives the shoreward flow in the upper layer over the inner shelf (water depth < 30 m).

In addition, the northeastward boundary current, a part of the South China Sea circulation in summer (Hu et al. 2000), is along the eastern coast of Hainan Island. The current-topography interaction drives the onshore transport that uplifts the UW to the upper layer (Lentz and Trowbridge 1991). Under the steady condition, the bottom Ekman transport relation (Brink and Lentz 2010) is given by $f U_{BE} = -\tau^y/\rho_0$, where the U_{BE} is the bottom Ekman transport controlled by the bottom along-shelf friction (τ^y). The cross-shelf transport can be one of interpretations for characteristics of the upwelling reflected by the spatial distribution of the relatively low temperature and high-salinity water at a depth of 20 m on the eastern shelf of Hainan Island and Leizhou Peninsula (Fig. 4).

5 Conclusions

We observed the HNEU in the summer cruise in 2009 and the HEU in the summer cruise in 2012. This study presents the comparison of the HEU and HNEU, and the analysis of the driving factors based on the hydrographic observation and reanalysis datasets: blended wind, SST, and precipitation. In order for water mass analysis, we construct the θ-S diagram based on the CTD data. The percentages of mixing ratio of three water masses (FW, UW, and SW) are calculated using the triangle of mixing method. It reveals that the HNEU was observed during the 2009 cruise when the southwesterly to southeasterly wind prevailed in the HNEU region, and the HEU occurred with the alongshore southwesterly wind during the 2012 cruise. To verify the general characteristics, we compute the composites of SST and wind for the three types of

Fig. 13 Profiles of the logarithmic TKE dissipation rates $\log_{10}[\varepsilon(\text{W kg}^{-1})]$ (*red curves*) and vertical diffusivity $\log_{10}[K_z(\text{m}^2\text{ s}^{-1})]$ (*blue bars*) at station C in 2009 (**a**) and 2012 (**b**), and station D in 2012 (**c**), respectively
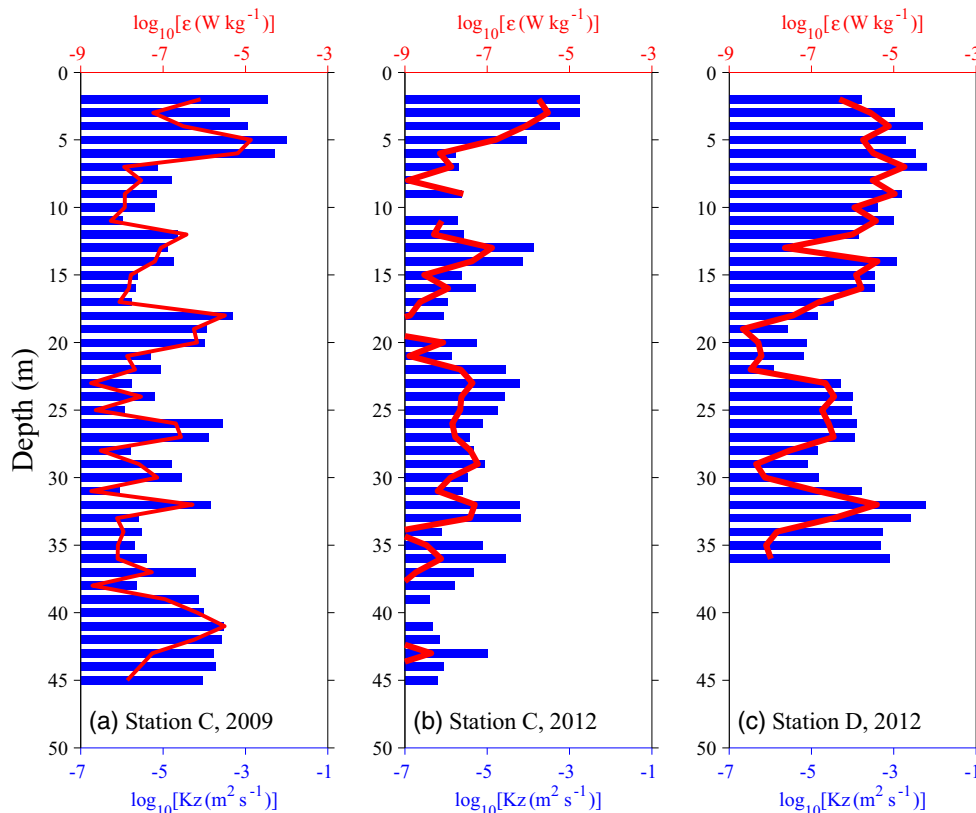
upwelling patterns (the intensified HEU, the intensified HNEU, and both HEU and HNEU in one day) based on the long-term reanalysis data. It again indicates that generally the HEU is southwesterly wind-driven, and the intensified HNEU is related to the southeasterly wind.

The rFW (the water mass mixed over 20 % FW) dominated the sea surface in the HNEU region, and formed the strong stratification with high buoyancy frequency; thus, UW cannot be uplifted continuously to the surface layer during the 2012 cruise. The precipitation composites for the three upwelling patterns display a general feature that the precipitation is close to zero around the HNEU region for the intensified HNEU pattern, but its extent southward extend to inhibit the HNEU in the surface for the intensified HEU pattern. In contrast, the turbulent mixing plays a positive role in enhancing the upwelling process. According to the vertical distribution of the TKE dissipation ε and the vertical diffusivity K_z estimated, the strong turbulent mixing could diffuse UW up to the surface. But, the freshwater and turbulent mixing did not remarkably impact on the HEU during either cruise.

In the study, however, the dynamical analysis of upwelling is limited by the lack of current data. It can be further identified by reasonable numerical modeling as well as the

extensive observations. For instance, Acoustic Doppler Current Profiler (ADCP) mooring data can be used to acquire the current velocity time series and the microstructure data from Microstructure Systems (MSS) Profiler will help to improve the present understanding.

Appendix: The triangle of mixing

Based on the water mass analysis method summarized by Mamayev (1975), on the *T-S* (or *θ-S*) diagram, the three water masses (e.g., A, B, and C, having temperatures and salinity T_A, S_A; T_B, S_B; T_C, S_C, respectively) form a triangle of mixing (Fig. 14). The product of the complete mixing of the three water masses will have a temperature and salinity determined by the formulae of mixing:
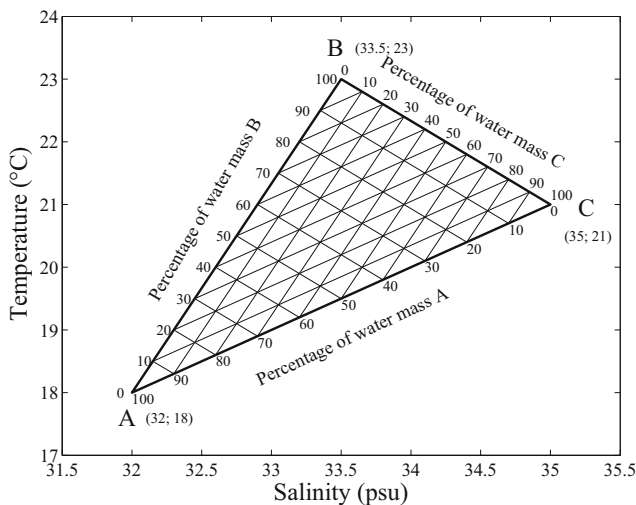
Fig. 14 An example of triangle of mixing, namely a nomogram for the determination of the percentage content of water masses. *A*, *B*, and *C* represent three water masses

$$T = aT_A + bT_B + cT_C, \tag{2}$$

$$S = aS_A + bS_B + cS_C, \tag{3}$$

$$a + b + c = 1, \tag{4}$$

where *a*, *b*, and *c* are the proportions of the three water masses. The points of mixing result of the three water masses lie within the triangle of mixing. In this study, the proportions *a*, *b*, and *c* are calculated by solving the formula system with the known temperature and salinity of the three water masses and the mixture.

The solution is:

$$a = -\frac{T(S_B - S_C) - S(T_B - T_C) + T_B S_C - T_C S_B}{T_A(S_B - S_C) - S_A(T_B - T_C) + T_B S_C - T_C S_B}, \tag{5}$$

$$b = -\frac{T(S_A - S_C) - S(T_A - T_C) + T_A S_C - T_C S_A}{T_A(S_B - S_C) - S_A(T_B - T_C) + T_B S_C - T_C S_B}, \tag{6}$$

$$c = -\frac{T(S_A - S_B) - S(T_A - T_B) + T_A S_B - T_B S_A}{T_A(S_B - S_C) - S_A(T_B - T_C) + T_B S_C - T_C S_B}. \tag{7}$$

References

Alford MH, MacKinnon JA, Nash JD, Simmons H, Pickering A, Klymak JM, Pinkel R, Sun O, Rainville L, Musgrave R, Beitzel T, Fu KH, Lu CW (2011) Energy flux and dissipation in Luzon Strait: two tales of two ridges. J Phys Oceanogr 41(11):2211–2222

Brink KH, Lentz SJ (2010) Buoyancy arrest and bottom Ekman transport part I: steady flow. J Phys Oceanogr 40(4):621–635

Chen Z, Yan X, Jo YH, Jiang L, Jiang Y (2012) A study of Benguela upwelling system using different upwelling indices derived from remotely sensed data. Cont Shelf Res 45:27–33

Dillon TM (1982) Vertical overturns: a comparison of Thorpe and Ozmidov length scales. J Geophys Res 87(C12):9601–9613

Galbraith PS, Kelley DE (1996) Identifying overturns in CTD profiles. J Atmos Ocean Technol 13:688–702

Gan J, Cheung A, Guo X, Li L (2009) Intensified upwelling over a widened shelf in the northeastern South China Sea. J Geophys Res 114, C09019. doi:10.1029/2007JC004660

Guo F, Shi M, Xia Z (1998) Two-dimension diagnose model to calculate upwelling on offshore of the east coast of Hainan Island. Acta Oceanol Sin 20(6):109–116 (in Chinese with English abstract)

Han Y, Wang M, Ma K (1990) The lowest surface water temperature area of China Sea in summer-the upwelling along the east coast of Hainan Island. Oceanol Et Limnol Sin 21(3):267–275 (in Chinese with English abstract)

Hu J, Kawamura H, Hong H, Qi Y (2000) A review on the currents in the South China Sea: seasonal circulation, South China Sea warm current and Kuroshio intrusion. J Oceanogr 56(6):607–624

Huffman GJ, Bolvin DT, Nelkin EJ, Wolff DB, Adler RF, Gu G, Hong Y, Bowman KP, Stocker EF (2007) The TRMM multisatellite precipitation analysis (TMPA): quasi-global, multiyear, combined-sensor precipitation estimates at fine scales. J Hydrometeorol 8(1):38–55

Jiang Y, Chai F, Wan Z, Zhang X, Hong H (2011) Characteristics and mechanisms of the upwelling in the southern Taiwan Strait: a three-dimensional numerical model study. J Oceanogr 67(6): 699–708

Jing Z, Qi Y, Hua Z, Zhang H (2009) Numerical study on the summer upwelling system in the northern continental shelf of the South China Sea. Cont Shelf Res 29(2):467–478

Jing Z, Qi Y, Du Y (2011) Upwelling in the continental shelf of northern South China Sea associated with 1997–1998 El Niño. J Geophys Res 116, C02033. doi:10.1029/2010JC006598

Klymak JM, Alford MH, Pinkel R, Lien RC, Yang YJ, Tang TY (2011) The breaking and scattering of the internal tide on a continental slope. J Phys Oceanogr 41(5):926–945

Lentz SJ, Fewings MR (2012) The wind-and wave-driven inner-shelf circulation. Ann Rev Mar Sci 4:317–343. doi:10.1146/annurev-marine-120709-142745

Lentz SJ, Trowbridge JH (1991) The bottom boundary layer over the northern California shelf. J Phys Oceanogr 21(8):1186–1201

Li L (1990) A study on the summer upwellings in shelf waters west to Zhujiang River mouth. J Oceanogr Taiwan Strait 9(4):338–346 (in Chinese with English abstract)

Li Y, Peng S, Yang W, Wang D (2012) Numerical simulation of the structure and variation of upwelling off the east coast of Hainan Island using QuikSCAT winds. Chin J Oceanol Limnol 30:1068–1081

Lin P, Cheng P, Gan J, Hu J (2016) Dynamics of wind-driven upwelling off the northeastern coast of Hainan Island. J Geophys Res Oceans 121. doi:10.1002/2015JC011000

Liu Z, Lozovatsky I (2012) Upper pycnocline turbulence in the northern South China Sea. Chin Sci Bull 57(18):2302–2306

Mamayev OI (1975) Temperature-salinity analysis of world oceans. Elsevier oceanography series, New york

Nash JD, Alford MH, Kunze E, Martini K, Kelly S (2007) Hotspots of deep ocean mixing on the Oregon continental slope. Geophys Res Lett 34, L01605. doi:10.1029/2006GL028170

Osborn TR (1980) Estimates of the local rate of vertical diffusion from dissipation measurements. J Phys Oceanogr 10:83–89

Song X, Lai Z, Ji R, Chen C, Zhang J, Huang L, Zhu X (2012) Summertime primary production in northwest South China Sea: interaction of coastal eddy, upwelling and biological processes. Cont Shelf Res 48:110–121

Sousa FM, Nascimento S, Casimiro H, Boutov D (2008) Identification of upwelling areas on sea surface temperature images using fuzzy clustering. Remote Sens Environ 112(6):2817–2823

Stansfield K, Garrett C, Dewey R (2001) The probability distribution of the Thorpe displacement within overturns in Juan de Fuca Strait. J Phys Oceanogr 31:3421–3434

Su J, Pohlmann T (2009) Wind and topography influence on an upwelling system at the eastern Hainan coast. J Geophys Res 114, C06017. doi:10.1029/2008JC005018

Su J, Wang J, Pohlmann T, Xu D (2011) The influence of meteorological variation on the upwelling system off eastern Hainan during summer 2007–2008. Ocean Dyn 61(6):717–730

Thorpe SA (1977) Turbulence and mixing in a Scottish loch. Philos Trans R Soc Lond 286A:125–181

Wang D, Wang H, Li M, Liu G, Wu X (2013) Role of Ekman transport versus Ekman pumping in driving summer upwelling in the South China Sea. J Ocean Univ China 12(3):355–365

Xie L, Zhang S, Zhao H (2012) Overview of studies on Qiongdong upwelling. J Trop Oceanogr 31(4):35–41 (in Chinese with English abstract)

Yu W (1987) A preliminary approach of the upwelling for the northern South China Sea. Mar Sci 6:7–10 (in Chinese with English abstract)

Zhang HM, Bates JJ, Reynolds RW (2006) Assessment of composite global sampling: sea surface wind speed. Geophys Res Lett 33, L17714. doi:10.1029/2006GL027086